

# Acidic Ultrafine Tungsten Oxide Molecular Wires for Cellulosic Biomass Conversion

Zhenxin Zhang,\* Masahiro Sadakane, Norihito Hiyoshi, Akihiro Yoshida, Michikazu Hara, and Wataru Ueda\*

**Abstract:** The application of nanocatalysis based on metal oxides for biomass conversion is of considerable interest in fundamental research and practical applications. New acidic transition-metal oxide molecular wires were synthesized for the conversion of cellulosic biomass. The ultrafine molecular wires were constructed by repeating  $(\text{NH}_4)_2[\text{XW}_6\text{O}_{21}]$  ( $X = \text{Te}$  or  $\text{Se}$ ) along the length, exhibiting diameters of only 1.2 nm. The nanowires dispersed in water and were observed using high-angle annular dark-field scanning transmission electron microscopy. Acid sites were created by calcination without collapse of the molecular wire structure. The acidic molecular wire exhibited high activity and stability and promoted the hydrolysis of the glycosidic bond. Various biomasses including cellulose were able to be converted to hexoses as main products.

The construction of molecular wires by polymerizing a molecular fragment in length direction while maintaining a molecular-level size in the other two dimensions has attracted much attention. Organic molecular wires are widely used.<sup>[1]</sup> However, inorganic molecular wires are rare and difficult to obtain.<sup>[2]</sup> The assembly of metal–oxygen octahedra is an ideal method for preparing well-crystallized solids based on a one-dimensional (1D) molecular structure.<sup>[3]</sup> Recent progress indicates that inorganic molecular wires can be obtained using a “top-down” approach, resulting in a new class of metal oxide molecular wires.<sup>[4]</sup> Therefore, this new field, although full of challenges, is receiving intense investigation.

Biomass utilization is important, owing to increasing attention on energy resource consumption for a sustainable society and development.<sup>[5]</sup> The condensation of glycosidic bonds forms a large class of cellulosic biomass, typically cellulose, and the conversion of cellulosic biomass into useful chemicals is one of the most important biomass conversion routes.<sup>[6]</sup> The first step is hydrolysis of a glycosidic bond to form hexoses, which can be further transformed to other chemicals. Brønsted acids are active for glycosidic bond hydrolysis. Various Brønsted acids have been utilized for the hydrolysis of cellulose, including traditional liquid acids and heteropoly acids<sup>[7]</sup> as homogeneous catalysts as well as carbon materials,<sup>[8,10]</sup> sulfonated resins,<sup>[9]</sup> zeolites,<sup>[10]</sup> solid super acids,<sup>[10]</sup> and transition-metal oxides<sup>[11]</sup> as heterogeneous catalysts. However, the current catalytic systems suffer from many problems that need to be overcome. These limitations include low catalytic activity, high catalyst loading, high reaction temperature, long reaction time, and difficulty with catalyst recycling.

A molecular wire based on metal oxide shows promise as solid acids owing to several advantages, such as nanosize, high stability, structure diversity, composition complexity, and tunable properties. The design and development of a metal oxide molecular wire with high acidity and stability are expected to exhibit high activity for catalytic cellulosic biomass conversion.

Herein, we report the successful design and synthesis of acidic solid molecular wires based on tungstotellurate (W-Te oxide) and tungstoselenate (W-Se oxide) and their application for cellulosic biomass conversion. The structure of the materials was confirmed by high-angle annular dark-field scanning transmission electron microscopy (HAADF-STEM) combined with other characterization techniques. Single molecular wires with a diameter of 1.2 nm were observed by electron microscopy and atomic force microscopy (AFM). W-Te oxide shows high thermal and hydrothermal stability and acted as a robust acid catalyst for hydrolysis of cellulosic biomass to produce hexoses.

The hydrothermal reaction of  $(\text{NH}_4)_6[\text{H}_2\text{W}_{12}\text{O}_{40}]$  and  $\text{TeO}_2$  or  $\text{SeO}_2$  under low pH conditions (ca. 1.5) resulted in gel-like yellow products, indicating that the particle size in the materials was small. The as-synthesized materials adsorbed a large amount of water. After the materials were dried at 80 °C, the volume of the material substantially decreased (Supporting Information, Figure S1). Powder X-ray diffraction (XRD) patterns exhibited broad peaks, indicating that the crystallinity of the materials was low (Figure 1). The precursor pH affected the resulting products. As shown in the Supporting Information, Figure S2, the W-Te oxide synthe-

[\*] Dr. Z. Zhang, Dr. A. Yoshida, Prof. Dr. W. Ueda  
Faculty of Engineering, Kanagawa University  
Rokkakubashi, Kanagawa-ku, Yokohama-shi, Kanagawa, 221-8686  
(Japan)  
E-mail: zhang.z.ag@m.titech.ac.jp  
uedaw@kanagawa-u.ac.jp

Dr. Z. Zhang, Prof. Dr. M. Hara  
Materials and Structures Laboratory, Tokyo Institute of Technology  
Nagatsuta-cho 4259, Midori-ku, Yokohama-city, Kanagawa, 226-8503  
(Japan)

Dr. M. Sadakane  
Department of Applied Chemistry, Hiroshima University  
1-4-1 Kagamiyama, Higashi Hiroshima 739-8527 (Japan)

Dr. N. Hiyoshi  
Research Institute for Chemical Process Technology, National  
Institute of Advanced Industrial Science and Technology (AIST)  
4-2-1 Nigatake, Miyagino, Sendai 983-8551 (Japan)

Supporting information for this article can be found under:  
<http://dx.doi.org/10.1002/anie.201602770>.

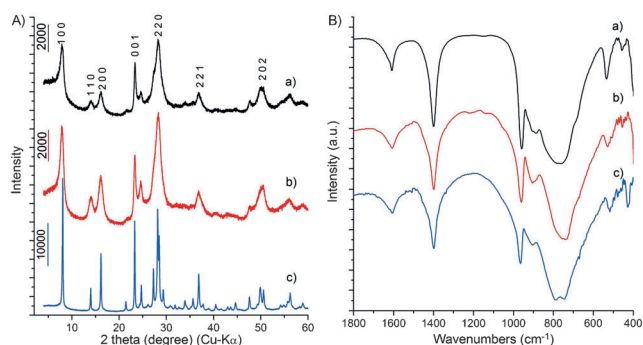
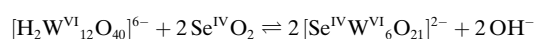
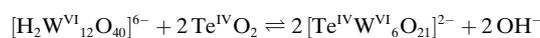


**Figure 1.** A) XRD patterns and B) FTIR spectra of a) W-Te oxide, b) W-Se oxide, and c) crystalline-W-Te oxide.

sized at a high pH (ca. 5) was a crystalline sample, denoted as crystalline-W-Te oxide. A decrease in the pH value of the precursor solution by less than 1.0 produced a material that had a different phase from that of W-Te oxide. For W-Se oxide, a high pH precursor did not yield a solid compound but a low pH yielded the same crystalline phase that was obtained for W-Te oxide.

The XRD pattern of the crystalline-W-Te oxide was indexed with a hexagonal cell ( $a = 12.6798 \text{ \AA}$ ,  $c = 3.8192 \text{ \AA}$ ), which was similar to that of Mo oxide molecular wire based crystals (Supporting Information, Figure S3).<sup>[4]</sup> The main XRD peaks of W-Te oxide and W-Se oxide can also be indexed to nearly the same unit cell, indicating that these materials have the same structure as that of crystalline-W-Te oxide (Figure 1A). The broad diffraction peaks of the materials may be due to the small size of the particles in the material. The particle size of the materials was estimated by Scherrer's equation, showing ca. 15 nm in length along the *c*-axis and ca. 9 nm in diameter across the *a*-*b* plane (Supporting Information, Figure S4). The FTIR spectra of W-Te oxide, W-Se oxide, and crystalline-W-Te oxide were identical (Figure 1B), and the FTIR spectra of the W-based oxide were similar to those of the Mo-based oxide (Supporting Information, Figure S3).<sup>[4]</sup> Therefore, the molecular structures of the materials were basically the same.

Elemental analysis indicated that the N:W:Te or Se ratio was 2:6:1. X-ray photoelectron spectroscopy (XPS; Supporting Information, Figure S5) showed that the W ions in both materials were  $\text{W}^{\text{VI}}$ , and the Te and Se ions were  $\text{Te}^{\text{IV}}$  and  $\text{Se}^{\text{IV}}$ , respectively, for the W-Te oxide and W-Se oxide, respectively. The UV/Vis spectra of the materials also indicated that the W ion in both materials was  $\text{W}^{\text{VI}}$ , because no absorbance between 500 and 800 nm was observed owing to the reduced W species (Supporting Information, Figure S6).<sup>[12]</sup> The chemical formulae for W-Te oxide and W-Se oxide were estimated to be  $(\text{NH}_4)_2[\text{Te}^{\text{IV}}\text{W}^{\text{VI}}_6\text{O}_{21}]$  and  $(\text{NH}_4)_2[\text{Se}^{\text{IV}}\text{W}^{\text{VI}}_6\text{O}_{21}]$ . The reactions for producing these materials can be expressed as follows:



The structure of crystalline-W-Te oxide was determined by the XRD pattern (Supporting Information, Tables S1–S3). The initial structure was refined by the Rietveld method. The simulated pattern was similar to the experimental pattern, indicating that the proposed structure was correct (Supporting Information, Figure S7).<sup>[4]</sup>

The structure was confirmed by HAADF-STEM.<sup>[13]</sup> The cross sectional image of the W-Te oxide (Figure 2a) shows

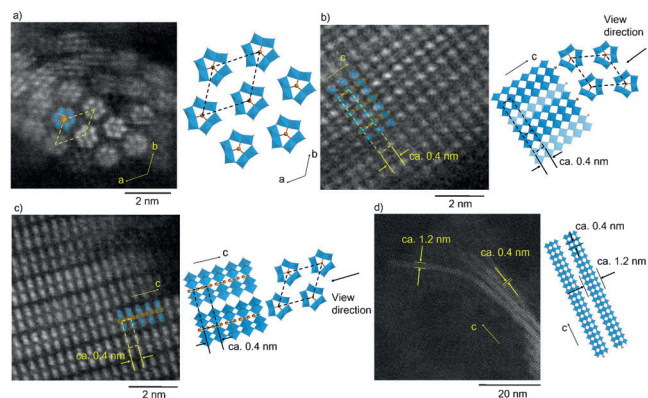


**Figure 2.** High-resolution HAADF-STEM images (left) and proposed structures (right) of a) W-Te oxide in the *a*-*b* plane, b) in the (100) plane, c) in the (2–10) plane, and d) W-Se oxide along the *c*-axis (dashed line indicates the unit cell; W blue, Te/Se brown, O red).

hexagonal units attributable to  $[\text{TeW}_6\text{O}_{21}]^{2-}$  and their hexagonal array with a periodicity of ca. 1.2 nm. The side views of W-Te oxide (Figure 2b,c) show that the hexagonal units are stacked with a layer distance of ca. 0.4 nm to form a molecular wire. The atomic positions observed in Figure 2a–c are in good agreement with the proposed structures (Figure 2 right) and that of crystalline-W-Te oxide. The side view of W-Se oxide (Figure 2d) also shows a lattice fringe with a spacing of ca. 0.4 nm owing to the stack of the hexagonal units ( $[\text{SeW}_6\text{O}_{21}]^{2-}$ ). A single molecular wire with a diameter of ca. 1.2 nm was observed in the end of a bundle of molecular wire.

The morphology of solid-state W-Te oxide and W-Se oxide was observed by scanning electron microscopy (SEM; Supporting Information, Figure S8). The crystalline-W-Te oxide had a uniform diameter of ca. 200 nm. The nanowire samples exhibited irregularly shaped particle aggregation.  $\text{N}_2$  adsorption–desorption measurement indicated the presence of nanoparticles in the solid states (Supporting Information, Figure S9). After dispersal, the surface areas of the materials are expected to increase substantially.

W-Te oxide and W-Se oxide easily formed nanowires by simply dispersing the samples in water by ultrasound or heating. The SEM and transmission electron microscopy (TEM) images show the ultrathin nanowires after dispersal in water (Figure 3; Supporting Information, Figure S10). Single molecular wires with diameters of about 1–2 nm can be easily obtained, as shown in the typical high-resolution (HR)-TEM images (Figure 3e,f).

The diameters of the materials after dispersal were further analyzed by AFM. The AFM images of the materials after

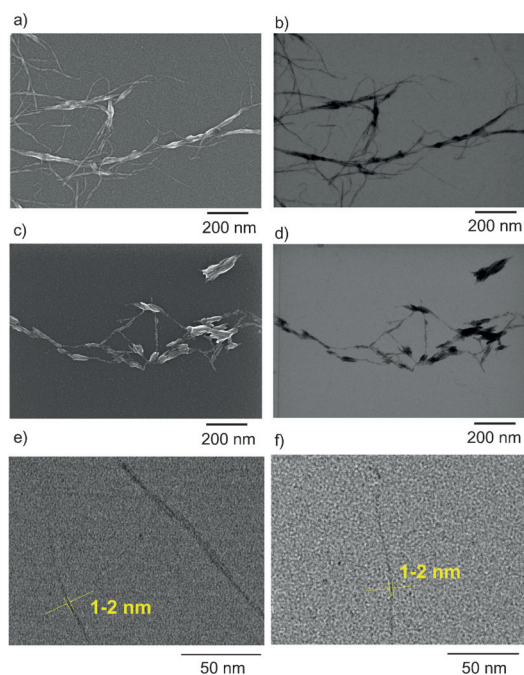


**Figure 3.** Electron microscopy images of the dispersed materials: a) SEM and b) TEM images of W-Te oxide; c) SEM and d) TEM images of W-Se oxide; HR-TEM images of e) W-Te oxide and f) W-Se oxide. The dispersed samples were prepared in water followed by sonication for 1 h, and then the solution was dropped on a TEM grid and dried.

dispersal indicated the presence of nanowires (Figure 4). In most cases, the nanowire consisted of an aggregation of several single molecular wires with a diameter less than 5 nm. A single molecular wire with the thickness of ca. 1.2 nm were also observed. All of the microscopy observations were conducted after the solution with the molecular wire was dried, and therefore particle aggregation could not be completely avoided.

FTIR spectra of the materials contained bands at ca. 1620 and 1400  $\text{cm}^{-1}$ , which correspond to  $\text{H}_2\text{O}$  and  $\text{NH}_4^+$ , respectively (Figure 1).  $\text{H}_2\text{O}$  and  $\text{NH}_4^+$  were near the molecular wires and could be removed by calcination. Thermogravi-

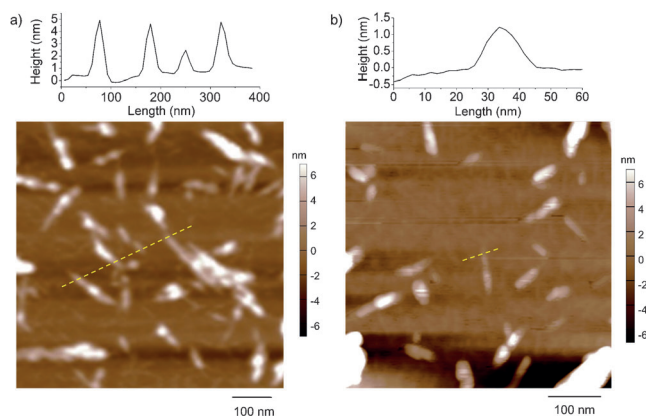


**Figure 4.** AFM images of a) W-Te oxide and b) W-Se oxide, top: thickness analysis indicated by yellow dashed lines in the AFM images. The sample was prepared using the same method as used for the TEM images.

metric-differential thermal analysis (TG-DTA) indicated that 8.5% and 10.7% weight losses were observed for W-Te oxide and W-Se oxide, respectively, during the heat treatment (Supporting Information, Figure S11). The desorption of  $\text{NH}_3$  ( $m/z = 16$ ) reached a peak maximum at 400 and 430  $^\circ\text{C}$  for W-Te oxide and W-Se oxide, respectively, in temperature-programmed desorption-mass spectrometry (TPD-MS; Supporting Information, Figure S12).

The thermal stability of W-Te oxide and W-Se oxide was evaluated. The materials were calcined under air at different temperatures for 2 h. W-Te oxide was stable at 350  $^\circ\text{C}$ . The XRD patterns and FTIR spectra (Supporting Information, Figure S13 a,b) of the materials calcined below 350  $^\circ\text{C}$  did not change. A further increase in the calcination temperature generated material that exhibited different XRD peaks and IR bands, which indicated damage to the original structure. For W-Se oxide, the thermal stability was lower than that of W-Te oxide. The material started to decompose at 300  $^\circ\text{C}$  (Supporting Information, Figure S13 c,d).

The amount of  $\text{NH}_3$  removed from W-Te oxide and W-Se oxide by calcination at 350  $^\circ\text{C}$  and 300  $^\circ\text{C}$ , respectively, was estimated by TPD-MS (Supporting Information, Figure S12), and the calcined samples are referred to W-Te-AC350 and W-Se-AC300, respectively. After calcination, about 50% of the  $\text{NH}_3$  was removed. We assume that desorption of  $\text{NH}_3$  from the material produced proton in the materials as acid sites. The chemical formulae of the calcined materials were estimated to be  $(\text{NH}_4)[\text{HTeW}_6\text{O}_{21}]$  and  $(\text{NH}_4)[\text{HSeW}_6\text{O}_{21}]$  for W-Te-AC350 and W-Se-AC300, respectively.

Hydrothermal stabilities of W-Te-AC350 and W-Se-AC300, were tested at 175  $^\circ\text{C}$  for 2 h. After the treatment, the dispersed materials were recovered by evaporating all of the  $\text{H}_2\text{O}$  (Supporting Information, Figure S14). W-Te-AC350 was stable, and the structure did not change after the hydrothermal treatment. By contrast, the structure of W-Se-AC300 changed under the same conditions.

W-Te-AC350 was characterized and used as an acid catalyst for biomass hydrolysis in an aqueous solution. TEM (Supporting Information, Figure S10 e,f) and AFM (Figure S15) images indicated that W-Te-AC350 formed well-dispersed nanowires after hydrothermal treatment. Size distribution based on TEM indicated that the distribution maximum for diameter and length was 2–3 nm and 40–60 nm, respectively (Figure S16). Oxidation states of W and Te were  $\text{W}^{\text{VI}}$  and  $\text{Te}^{\text{IV}}$  (Figure S5). Elemental analysis and TG-DTA (Figure S11 c) showed the ratio N:W:Te was 1:6:1, which was identical to the formula of  $(\text{NH}_4)[\text{HTe}^{\text{IV}}\text{W}_6^{\text{VI}}\text{O}_{21}]\cdot 2\text{H}_2\text{O}$ . Using  $\text{NH}_3$  as a probe molecule combined with TPD showed that the acid amount of the material was 0.41  $\text{mmol g}^{-1}$  in solid state (Figure S17). Titration showed that the acid concentration of the dispersed material was 0.80  $\text{mmol g}^{-1}$ .

As shown in Table 1, cellobiose was hydrolyzed by W-Te-AC350 at 130  $^\circ\text{C}$  for 4 h under hydrothermal conditions, and glucose was obtained as the main product with a high yield (90.5%). Other soluble polysaccharides, such as sucrose and starch, were converted into glucose under the same conditions (Table 1, entries 2,3). Compared with the reported catalyst, W-Te-AC350 exhibited high activity for hydrolysis of poly-

**Table 1:** Biomass hydrolysis by W-Te-AC350 under different conditions.<sup>[a]</sup>

Entry	Biomass	t [h]	T [°C]	Conversion [%]	Yield based on carbon [%]				Total yield of organics [%]	
					glucose	mannose	formic acid	levulinic acid		HMF
1	cellobiose	4	130	93.1	90.5	0	0.1	0.1	0.7	91.4
2	sucrose	4	130	99	43.9	1.9	3.3	15.1	7.8	72.0
3	starch	4	130	–	78.4	0.2	0.5	1.0	1.2	81.3
4	microcrystalline cellulose <sup>[b]</sup>	2	175	–	8.8	2.9	0.5	1.1	0.7	14.0
5	ball-milled cellulose	2	175	–	19.0	7.2	0.7	2.5	1.2	30.6
6	ball-milled cellulose <sup>[c]</sup>	2	175	–	25.8	7.8	3.0	8.5	2.0	47.1
7	microcrystalline cellulose <sup>[d]</sup>	2	175	–	0	0	0	0	0	0

[a] Reaction conditions: biomass: 0.308 mmol based on glucose unit, W-Te-AC350: 0.05 g, water 0.5 mL. [b] Carbon balance was 86.7% (see details in the Supporting Information). [c] cellulose: 0.185 mmol. [d] Without catalyst.

saccharides (Supporting Information, Tables S4 and S5). Cellulose is more difficult to convert and was hydrolyzed at 175 °C for 2 h. Hexoses (glucose and mannose) were the primary products. Some other products were detected, such as 5-hydroxymethylfurfural (HMF), levulinic acid, and formic acid. Ball-milling can decrease the crystallinity of cellulose (Supporting Information, Figure S18) and activate the cellulose.<sup>[14]</sup> The activity of the reaction increased using the ball-milled cellulose (Table 1, entries 5,6). In the absence of the catalyst, no products were detected (Table 1, entry 7).

The catalytic activities of different materials were investigated for comparison with W-Te-AC350. As shown in the Supporting Information, Table S6, under the same conditions, W-Te-AC350 was more active for microcrystalline cellulose conversion than other solid acids based on the amount of acid. Moreover, the activity of W-Te-AC350 was comparable to homogeneous catalysts (Supporting Information, Table S6).

The calcination temperature affected the catalytic activity of W-Te-AC350. As shown in the Supporting Information, Figure S19, the as-synthesized material exhibited low activity, and an increase in the calcination temperature enhanced the activity. When the calcination was conducted at 350 °C, the highest activity was obtained. This result demonstrated that acid sites were generated by calcination. However, a further increase in the calcination temperature (400 °C) deactivated the catalyst, which was most likely due to structural decomposition of the material at a high temperature. Therefore, maintaining the nanowire structure is a key factor for high catalytic activity.

The catalyst concentration was investigated. As the catalyst concentration increased, the total detected products increased, and hexoses tended to be further converted into other products, such as levulinic acid and formic acid. A decrease in the catalyst concentration effectively increased the selectivity to hydrolysis products (Supporting Information, Figure S20). Prolonging the reaction time yielded more organic acids and HMF, although the total yield of detected products increased (Supporting Information, Figure S21). A decrease in the reaction temperature decreased the activity and effectively suppressed the conversion of the generated hexoses. The selectivity to hexose increased at a low reaction temperature (Supporting Information, Figure S22).

The catalyst can be reused. Elemental analysis indicated that 47% of the catalyst was recovered by a low-speed centrifugation (9800 G, 1 h). The activity of the catalyst was

low (Supporting Information, Figure S23). TEM (Supporting Information, Figure S10i,j) and the size distribution (Supporting Information, Figure S16) indicated that some nanowires were still in the solution. When a high-speed centrifugation condition (48000 G, 24 h) was used, a higher activity of the recovered catalyst was achieved.

The high catalytic activity of W-Te-AC350 was primarily due to two factors: ultrafine nanosized catalyst particles after dispersal and the strong interactions between the catalyst and the biomass. W-Te-AC350 could be well dispersed in water under hydrothermal conditions (175 °C, 2 h). After the hydrothermal treatment, the photographic images indicated that the solution containing the material became transparent and exhibited laser scattering, which indicated that the material dispersed and formed ultrafine nanowires in water (Supporting Information, Figure S24 a,b). For a sample with a low concentration, the laser scattering phenomenon still existed after the hydrothermal treatment (Figure S24 c,d), indicating that the material was not dissolved in water but dispersed. Before and after the hydrothermal treatment, dynamic light scattering (DLS) was conducted for W-Te-AC350, and the results revealed that after the hydrothermal treatment, the particle size of the material decreased (Supporting Information, Figure S25). The SEM and TEM images (Figure S10 e,f) revealed that W-Te-AC350 remained a nanowire. After the hydrothermal treatment, W-Te-AC350 was dried at –30 °C under high vacuum. The surface area of the dispersed W-Te-AC350 (15 m<sup>2</sup>g<sup>–1</sup>) was higher than that of the as-synthesized W-Te oxide (Supporting Information, Figure S9). The adsorption under low pressure demonstrated the existence of micropores that may be due to the gap formed by isolated molecular wires. The calcined crystalline-W-Te oxide (Supporting Information, Figure S26) exhibited a lower activity than that of W-Te-AC350, which indicated that the nanosized material exhibited improved activity for the reaction (Supporting Information, Table S6, entry 2). All of the results demonstrated that the hydrothermal treatment promoted dispersal of the material in water and increase in the surface area.

Four oxygen sites are present in W-Te-AC350, including corner-sharing oxygen (O1), edge-sharing oxygen (O2), layer-sharing oxygen (O3), and terminal oxygen (O4), for protonation without considering the interactions between protons with NH<sub>4</sub><sup>+</sup> (Supporting Information, Figure S27). When O2 was protonated, the system energy was the lowest among all

of the models, which indicated that O2 was the most likely position for protonation. The interaction between cellulose and the materials was simulated using cellobiose as a model molecule. The hexagonal unit with protonated O2 was used as a model for the catalyst. A Monte Carlo simulation (Supporting Information, Figure S28) showed that cellobiose interacted with the lattice oxygen,  $\text{NH}_4^+$ , and the proton of the molecular wire with the distance between O and H shorter than 3 Å, indicating that strong or medium hydrogen bonds existed between the catalyst and cellobiose. The interaction between W-Te-AC350 and cellobiose was investigated using  $^1\text{H}$  NMR (Supporting Information, Figure S29). When only cellobiose was present, peaks corresponding to the hydroxyl groups of cellobiose were observed by  $^1\text{H}$  NMR.<sup>[15]</sup> After the addition of W-Te-AC350 to the cellobiose solution, the peaks corresponding to hydroxyl group of cellobiose was broadened, indicating fast proton exchange between the molecular wire (W-OH) and cellobiose (-OH) as well as the existence of an interaction between the catalyst and the biomass.

In summary, an acidic nanocatalyst based on a W-oxide molecular wire was synthesized and characterized. The structure of the molecular wire was confirmed using an atomic-resolution HAADF-STEM image combined with XRD, FTIR, XPS, TPD, TG, and elemental analysis, and the result indicated that the growth of a hexagonal unit,  $(\text{NH}_4)_2[\text{TeW}_6\text{O}_{21}]$  or  $(\text{NH}_4)_2[\text{SeW}_6\text{O}_{21}]$ , resulted in the formation of an inorganic 1D polymer. W-Te oxide exhibited high thermal and hydrothermal stability and was acidified by calcination. The acidic molecular wire was dispersed in water and acted as an efficient catalyst for biomass hydrolysis to produce hexoses.

### Acknowledgements

This work was supported in part by the Novel Cheap and Abundant Materials for Catalytic Biomass Conversion (NOVACAM, FP7-NMP-2013-EU-Japan-604319) program of the Japan Science and Technology Agency (JST). The authors also thank Professor Atsushi Kameyama for the DLS analysis and the Material Analysis Suzukake-dai Center, Technical Department, Tokyo Institute of Technology, for the elemental analysis and NMR measurement.

**Keywords:** cellulosic biomass · hexose · hydrolysis · molecular wires · tungsten oxide

- [1] a) W. B. Davis, W. A. Svec, M. A. Ratner, M. R. Wasielewski, *Nature* **1998**, *396*, 60–63; b) H. Sakaguchi, H. Matsumura, H. Gong, *Nat. Mater.* **2004**, *3*, 551–557; c) C. M. Gothard, N. A. Rao, J. S. Nowick, *J. Am. Chem. Soc.* **2007**, *129*, 7272–7273; d) R. N. Mahato, H. Lülfi, M. H. Siekman, S. P. Kersten, P. A. Bobbert, M. P. de Jong, L. De Cola, W. G. van der Wiel, *Science* **2013**, *341*, 257–260.
- [2] M. Remskar, A. Mrzel, Z. Skraba, A. Jesih, M. Ceh, J. Demsar, P. Stadelmann, F. Levy, D. Mihailovic, *Science* **2001**, *292*, 479–481.
- [3] a) J. R. Galán-Mascarós, C. Giménez-Saiz, S. Triki, C. J. Gómez-García, E. Coronado, L. Ouahab, *Angew. Chem. Int. Ed. Engl.* **1995**, *34*, 1460–1462; *Angew. Chem.* **1995**, *107*, 1601–1603; b) L. Chen, D. Shi, J. Zhao, Y. Wang, P. Ma, J. Wang, J. Niu, *Cryst. Growth Des.* **2011**, *11*, 1913–1923; c) Y. Wang, S. Pan, H. Yu, X. Su, M. Zhang, F. Zhang, J. Han, *Chem. Commun.* **2013**, *49*, 306–308.
- [4] Z. Zhang, T. Murayama, M. Sadakane, H. Ariga, N. Yasuda, N. Sakaguchi, K. Asakura, W. Ueda, *Nat. Commun.* **2015**, *6*, 7731.
- [5] a) C. O. Tuck, E. Pérez, I. T. Horváth, R. A. Sheldon, M. Poliakoff, *Science* **2012**, *337*, 695–699; b) A. Wang, T. A. O. Zhang, *Acc. Chem. Res.* **2013**, *46*, 1377–1386; c) R. Rinaldi, F. Schüth, *Energy Environ. Sci.* **2009**, *2*, 610–626.
- [6] a) Y.-B. Huang, Y. Fu, *Green Chem.* **2013**, *15*, 1095–1111; b) T. Salmi, B. Holmbom, S. Willf, D. Y. Murzin, *Chem. Rev.* **2011**, *111*, 5638–5666; c) K. Shimizu, A. Satsuma, *Energy Environ. Sci.* **2011**, *4*, 3140–3153; d) H. Tadesse, R. Luque, *Energy Environ. Sci.* **2011**, *4*, 3913–3929.
- [7] a) K. Shimizu, H. Furukawa, N. Kobayashi, Y. Itaya, A. Satsuma, *Green Chem.* **2009**, *11*, 1627–1632; b) W. Deng, Q. Zhang, Y. Wang, *Dalton Trans.* **2012**, *41*, 9817–9831.
- [8] a) H. Kobayashi, M. Yabushita, J. Hasegawa, A. Fukuoka, *J. Phys. Chem. C* **2015**, *119*, 20993–20999; b) L. Shuai, X. Pan, *Energy Environ. Sci.* **2012**, *5*, 6889–6894; c) S. Suganuma, K. Nakajima, M. Kitano, D. Yamaguchi, H. Kato, S. Hayashi, M. Hara, *J. Am. Chem. Soc.* **2008**, *130*, 12787–12793; d) H. Kobayashi, H. Kaiki, A. Shrotri, K. Techikawara, A. Fukuoka, *Chem. Sci.* **2016**, *7*, 692–696.
- [9] R. Rinaldi, R. Palkovits, F. Schüth, *Angew. Chem. Int. Ed.* **2008**, *47*, 8047–8050; *Angew. Chem.* **2008**, *120*, 8167–8170.
- [10] A. Onda, T. Ochi, K. Yanagisawa, *Green Chem.* **2008**, *10*, 1033–1037.
- [11] A. Takagaki, C. Tagusagawa, K. Domen, *Chem. Commun.* **2008**, 5363–5365.
- [12] K. Fukuda, K. Akatsuka, Y. Ebina, R. Ma, K. Takada, I. Nakai, T. Sasaki, *ACS Nano* **2008**, *2*, 1689–1695.
- [13] N. Hiyoshi, Y. Kamiya, *Chem. Commun.* **2015**, *51*, 9975–9978.
- [14] a) C. F. Burmeister, A. Kwade, *Chem. Soc. Rev.* **2013**, *42*, 7660–7667; b) A. Shrotri, L. K. Lambert, A. Tanksale, J. Beltrami, *Green Chem.* **2013**, *15*, 2761–2768.
- [15] B. Bernet, R. Bürli, J. Xu, A. Vasella, *Helv. Chim. Acta* **2002**, *85*, 1800–1811.

Received: March 19, 2016

Revised: June 20, 2016

Published online: ■ ■ ■ ■ ■, ■ ■ ■ ■ ■

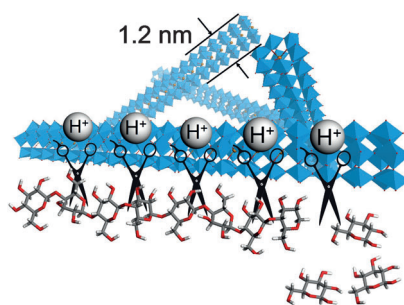
## Communications



## Molecular Wires

Z. Zhang,\* M. Sadakane, N. Hiyoshi,  
A. Yoshida, M. Hara,  
W. Ueda\* ————— ■■■■-■■■■

Acidic Ultrafine Tungsten Oxide  
Molecular Wires for Cellulosic Biomass  
Conversion



A **molecular wire** based on tungsten oxide with a diameter of 1.2 nm was synthesized. Acid sites were created in aqueous solution by calcination without collapse of the molecular wire structure. This material was applied for the hydrolysis of cellulosic biomass to produce hexose.